

# Laboratory Experimentation of Guidance and Control of Spacecraft During On-orbit Proximity Maneuvers

Jason S. Hall and Marcello Romano  
*Naval Postgraduate School  
Monterey, CA, USA*

## 1. Introduction

The traditional spacecraft system is a monolithic structure with a single mission focused design and lengthy production and qualification schedules coupled with enormous cost. Additionally, there rarely, if ever, is any designed preventive maintenance plan or re-fueling capability. There has been much research in recent years into alternative options. One alternative option involves autonomous on-orbit servicing of current or future monolithic spacecraft systems. The U.S. Department of Defense (DoD) embarked on a highly successful venture to prove out such a concept with the Defense Advanced Research Projects Agency's (DARPA's) Orbital Express program. Orbital Express demonstrated all of the enabling technologies required for autonomous on-orbit servicing to include refueling, component transfer, autonomous satellite grappling and berthing, rendezvous, inspection, proximity operations, docking and undocking, and autonomous fault recognition and anomaly handling (Kennedy, 2008). Another potential option involves a paradigm shift from the monolithic spacecraft system to one involving multiple interacting spacecraft that can autonomously assemble and reconfigure. Numerous benefits are associated with autonomous spacecraft assemblies, ranging from a removal of significant intra-modular reliance that provides for parallel design, fabrication, assembly and validation processes to the inherent smaller nature of fractionated systems which allows for each module to be placed into orbit separately on more affordable launch platforms (Mathieu, 2005).

With respect specifically to the validation process, the significantly reduced dimensions and mass of aggregated spacecraft when compared to the traditional monolithic spacecraft allow for not only component but even full-scale on-the-ground Hardware-In-the-Loop (HIL) experimentation. Likewise, much of the HIL experimentation required for on-orbit servicing of traditional spacecraft systems can also be accomplished in ground-based laboratories (Creamer, 2007). This type of HIL experimentation complements analytical methods and numerical simulations by providing a low-risk, relatively low-cost and potentially high-return method for validating the technology, navigation techniques and control approaches associated with spacecraft systems. Several approaches exist for the actual HIL testing in a laboratory environment with respect to spacecraft guidance, navigation and control. One

such method involves reproduction of the kinematics and vehicle dynamics for 3-DoF (two horizontal translational degrees and one rotational degree about the vertical axis) through the use of robotic spacecraft simulators that float via planar air bearings on a flat horizontal floor. This particular method is currently being employed by several research institutions and is the validation method of choice for our research into GNC algorithms for proximity operations at the Naval Postgraduate School (Machida et al., 1992; Ullman, 1993; Corrazzini & How, 1998; Marchesi et al., 2000; Ledebuhr et al., 2001; Nolet et al., 2005; LeMaster et al., 2006; Romano et al., 2007). With respect to spacecraft involved in proximity operations, the in-plane and cross-track dynamics are decoupled, as modeled by the Hill-Clohessy-Wiltshire (HCW) equations, thus the reduction to 3-Degree of Freedom (DoF) does not appear to be a critical limiter. One consideration involves the reduction of the vehicle dynamics to one of a double integrator. However, the orbital dynamics can be considered to be a disturbance that needs to be compensated for by the spacecraft navigation and control system during the proximity navigation and assembly phase of multiple systems. Thus the flat floor testbed can be used to capture many of the critical aspects of an actual autonomous proximity maneuver that can then be used for validation of numerical simulations. Portions of the here-in described testbed, combined with the first generation robotic spacecraft simulator of the Spacecraft Robotics Laboratory (SRL) at Naval Postgraduate School (NPS), have been employed to propose and experimentally validate control algorithms. The interested reader is referred to (Romano et al., 2007) for a full description of this robotic spacecraft simulator and the associated HIL experiments involving its demonstration of successful autonomous spacecraft approach and docking maneuvers to a collaborative target with a prototype docking interface of the Orbital Express program.

Given the requirement for spacecraft aggregates to rendezvous and dock during the final phases of assembly and a desire to maximize the useable surface area of the spacecraft for power generation, sensor packages, docking mechanisms and payloads while minimizing thruster impingement, control of such systems using the standard control actuator configuration of fixed thrusters on each face coupled with momentum exchange devices can be challenging if not impossible. For such systems, a new and unique configuration is proposed which may capitalize, for instance, on the recently developed carpal robotic joint invented by Dr. Steven Canfield with its hemispherical vector space (Canfield, 1998). It is here demonstrated through Lie algebra analytical methods and experimental results that two vectorable in-plane thrusters in an opposing configuration can yield a minimum set of actuators for a controllable system. It will also be shown that by coupling the proposed set of vectorable thrusters with a single degree of freedom Control Moment Gyroscope, an additional degree of redundancy can be gained. Experimental results are included using SRL's second generation reduced order (3 DoF) spacecraft simulator. A general overview of this spacecraft simulator is presented in this chapter (additional details on the simulators can be found in: Hall, 2006; Eikenberry, 2006; Price, W., 2006; Romano & Hall, 2006; Hall & Romano, 2007a; Hall & Romano, 2007b).

While presenting an overview of a robotic testbed for HIL experimentation of guidance and control algorithms for on-orbit proximity maneuvers, this chapter specifically focuses on exploring the feasibility, design and evaluation in a 3-DoF environment of a vectorable thruster configuration combined with optional miniature single gimballed control moment gyro (MSGCMG) for an agile small spacecraft. Specifically, the main aims are to present and practically confirm the theoretical basis of small-time local controllability for this unique

actuator configuration through both analytical and numerical simulations performed in previous works (Romano & Hall, 2006; Hall & Romano, 2007a; Hall & Romano, 2007b) and to validate the viability of using this minimal control actuator configuration on a small spacecraft in a practical way. Furthermore, the experimental work is used to confirm the controllability of this configuration along a fully constrained trajectory through the employment of a smooth feedback controller based on state feedback linearization and linear quadratic regulator techniques and proper state estimation methods. The chapter is structured as follows: First the design of the experimental testbed including the floating surface and the second generation 3-DoF spacecraft simulator is introduced. Then the dynamics model for the spacecraft simulator with vectorable thrusters and momentum exchange device are formulated. The controllability concerns associated with this uniquely configured system are then addressed with a presentation of the minimum number of control inputs to ensure small time local controllability. Next, a formal development is presented for the state feedback linearized controller, state estimation methods, Schmitt trigger and Pulse Width Modulation scheme. Finally, experimental results are presented.

## **2. The NPS Robotic Spacecraft Simulator Testbed**

Three generations of robotic spacecraft simulators have been developed at the NPS Spacecraft Robotics Laboratory, in order to provide for relatively low-cost HIL experimentation of GNC algorithms for spacecraft proximity maneuvers (see Fig.1). In particular, the second generation robotic spacecraft simulator testbed is used for the here-in presented research. The whole spacecraft simulator testbed consists of three components. The two components specifically dedicated to HIL experimentation in 3-DoF are a floating surface with an indoor pseudo-GPS (iGPS) measurement system and one 3-DoF autonomous spacecraft simulator. The third component of the spacecraft simulator testbed is a 6-DoF simulator stand-alone computer based spacecraft simulator and is separated from the HIL components. Additionally, an off-board desktop computer is used to support the 3-DoF spacecraft simulator by providing the capability to upload software, initiate experimental testing, receive logged data during testing and process the iGPS position coordinates. Fig. 2 depicts the robotic spacecraft simulator in the Proximity Operations Simulator Facility (POSF) at NPS with key components identified. The main testbed systems are briefly described in the next sections with further details given in (Hall, 2006; Price, 2006; Eikenberry, 2006; Romano & Hall, 2006; Hall & Romano, 2007a; Hall & Romano 2007b).



Fig. 1. Three generations of spacecraft simulator at the NPS Spacecraft Robotics Laboratory (first, second and third generations from left to right)

### 2.1 Floating Surface

A 4.9 m by 4.3 m epoxy floor surface provides the base for the floatation of the spacecraft simulator. The use of planar air bearings on the simulator reduces the friction to a negligible level and with an average residual slope angle of approximately  $2.6 \times 10^{-3}$  deg for the floating surface, the average residual acceleration due to gravity is approximately  $1.8 \times 10^{-3} \text{ ms}^{-2}$ . This value of acceleration is 2 orders of magnitude lower than the nominal amplitude of the measured acceleration differences found during reduced gravity phases of parabolic flights (Romano et al, 2007).

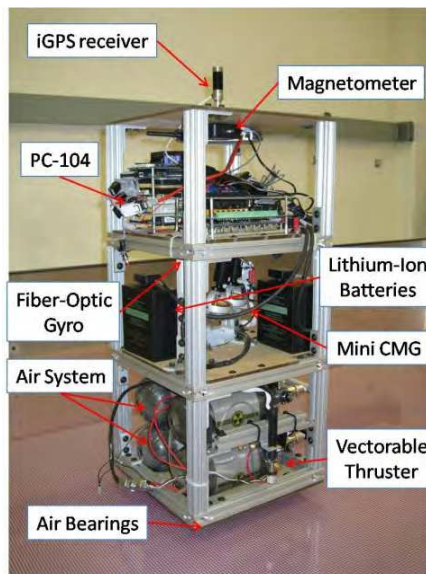


Fig. 2. SRL's 2nd Generation 3-DoF Spacecraft Simulator

## **2.2 3-DoF Robotic Spacecraft Simulator**

SRL's second generation robotic spacecraft simulator is modularly constructed with three easily assembled sections dedicated to each primary subsystem. Prefabricated 6105-T5 Aluminum fractional t-slotted extrusions form the cage of the vehicle while one square foot, .25 inch thick static dissipative rigid plastic sheets provide the upper and lower decks of each module. The use of these materials for the basic structural requirements provides a high strength to weight ratio and enable rapid assembly and reconfiguration. Table 1 reports the key parameters of the 3-DoF spacecraft simulator.

### **2.2.1 Propulsion and Flotation Subsystems**

The lowest module houses the flotation and propulsion subsystems. The flotation subsystem is composed of four planar air bearings, an air filter assembly, dual 4500 PSI (31.03 MPa) carbon-fiber spun air cylinders and a dual manifold pressure reducer to provide 75 PSI (.51 MPa). This pressure with a volume flow rate for each air bearing of 3.33 slfm ( $3.33 \times 10^{-3} \text{ m}^3/\text{min}$ ) is sufficient to keep the simulator in a friction-free state for nearly 40 minutes of continuous experimentation time. The propulsion subsystem is composed of dual vectorable supersonic on-off cold-gas thrusters and a separate dual carbon-fiber spun air cylinder and pressure reducer package regulated at 60 PSI (.41 MPa) and has the capability of providing the system  $31.1 \text{ m/s } \Delta V$ .

### **2.2.2 Electronic and Power Distribution Subsystems**

The power distribution subsystem is composed of dual lithium-ion batteries wired in parallel to provide 28 volts for up to 12 Amp-Hours and is housed in the second deck of the simulator. A four port DC-DC converter distributes the requisite power for the system at 5, 12 or 24 volts DC. An attached cold plate provides heat transfer from the array to the power system mounting deck in the upper module. The current power requirements include a single PC-104 CPU stack, a wireless router, three motor controllers, three separate normally-closed solenoid valves for thruster and air bearing actuation, a fiber optic gyro, a magnetometer and a wireless server for transmission of the vehicle's position via the pseudo-GPS system.

Subsystem	Characteristic	Parameter
Structure	Length and width	.30 m
	Height	.69 m
	Mass (Overall)	26 kg
	$J_z$ (Overall)	.40 kg-m <sup>2</sup>
Propulsion	Propellant	Compressed Air
	Equiv. storage capacity	.05 m <sup>3</sup> @ 31.03 Mpa
	Operating pressure	.41 Mpa
	Thrust (x2)	.159 N
	ISP	34.3 s
	Total $\Delta V$	31.1 m/s
Flotation	Propellant	Air
	Equiv. storage capacity	0.05 m <sup>3</sup> @ 31.03 Mpa
	Operating pressure	.51 Mpa
	Linear air bearing (x4)	32 mm diameter
	Continuous operation	~40 min
CMG Attitude Control	Max torque	.668 Nm
	Momentum storage	.098 Nms
Electrical & Electronic	Battery type	Lithium-Ion
	Storage capacity	12 Ah @ 28V
	Continuous Operation	~6 h
	Computer	1 PC104 Pentium III
Sensors	Fiber optic gyro	KVH Model DSP-3000
	Position sensor	Metris iGPS
	Magnetometer	MicroStrain 3DM-GX1

Table 1. Key Parameters of the 2nd generation 3-DoF Robotic Spacecraft Simulator

### 2.2.3 Translation and Attitude Control System Actuators

The 3-DoF robotic spacecraft simulator includes actuators to provide both translational control and attitude control. A full development of the controllability for this unique configuration of dual rotating thrusters and one-axis Miniature-Single Gimbaled Control Moment Gyro (MSGCMG) will be demonstrated in subsequent sections of this paper. The translational control is provided by two cold-gas on-off supersonic nozzle thrusters in a dual vectorable configuration. Each thruster is limited in a region  $\pm\pi/2$  with respect to the face normal and, through experimental testing at the supplied pressure, has been demonstrated to have an ISP of 34.3 s and able to provide .159 N of thrust with less than 10 msec actuation time (Lugini, 2008). The MSGCMG is capable of providing .668 Nm of torque with a maximum angular momentum of .098 Nms.

### 2.3 6-DoF Computer-Based Numerical Spacecraft Simulator

A separate component of SRL's spacecraft simulator testbed at NPS is a 6-DoF computer-based spacecraft simulator. This simulator enables full 6-DoF numerical simulations to be conducted with realistic orbital perturbations including aerodynamic, solar pressure and

third-body effects, and earth oblateness up to J4. Similar to the 3-DoF robotic simulator, the numerical simulator is also modularly designed within a MATLAB®/Simulink® architecture to allow near seamless integration and testing of developed guidance and control algorithms. Additionally, by using the MATLAB®/Simulink® architecture with the added Real Time Workshop™ toolbox, the developed control algorithms can be readily transitioned into C-code for direct deployment onto the 3-DoF robotic simulator's onboard processor. A full discussion of the process by which this is accomplished and simplified for rapid real-time experimentation on the 3-DoF testbed for either the proprietary MATLAB® based XPCTarget™ operating system is given in (Hall, 2006; Price, 2006) or for an open-source Linux based operating system with the Real Time Application Interface (RTAI) is given in (Bevilacqua et al., 2009).

### 3. Dynamics of a 3-DoF Spacecraft Simulator with Vectorable Thrusters and Momentum Exchange Device

Two sets of coordinate frame are established for reference: the inertial coordinate system (ICS) designated by  $XYZ$  and body-fixed coordinate system (BCS) designated by  $xyz$ . These reference frames are depicted in **Fig. 3** along with the necessary external forces and parameters required to properly define the simulator's motion. The origin of the body-fixed coordinate system is taken to be the center of mass  $C$  of the spacecraft simulator and this is assumed to be collocated with the simulator's geometric center. The body  $z$ -axis is aligned with the inertial  $Z$ -axis while the body  $x$ -axis is in line with the thrusters points of action. In the ICS, the position and velocity vectors of  $C$  are given by  $\mathbf{X}$  and  $\mathbf{V}$  so that  $\mathbf{X}(X, Y)$  marks the position of the simulator with respect to the origin of the ICS as measured by the inertial measurement sensors and provides the vehicle's two degrees of translational freedom. The vehicle's rotational freedom is described by an angle of rotation  $\psi$  between the  $x$ -axis and the  $X$ -axis about the  $z$ -axis. The angular velocity is thus limited to one degree of freedom and is denoted by  $\omega_z$ . The spacecraft simulator is assumed to be rigid and therefore a constant moment of inertia ( $J_z$ ) exists about the  $z$ -axis. Furthermore, any changes to the mass of the simulator ( $m$ ) due to thruster firing are neglected.

The forces imparted at a distance  $L$  from the center of mass by the vectorable on-off thrusters are denoted by  $F_1$  and  $F_2$  respectively. The direction of the thrust vector  $\mathbf{F}_1$  is determined by  $\alpha_1$  which is the angle measured from the outward normal of face one in a clockwise direction (right-hand rotation) to where thruster one's nozzle is pointing. Likewise, the direction of the thrust vector  $\mathbf{F}_2$  is determined by  $\alpha_2$  which is the angle measured from the outward normal of face two in a clockwise direction (right-hand rotation) to where thruster two's nozzle is pointing. The torque imparted on the vehicle by a momentum exchange device such as a control moment gyro is denoted by  $T_{MED}$  and can be constrained to exist only about the yaw axis as demonstrated in (Hall, 2006; Romano & Hall, 2006).

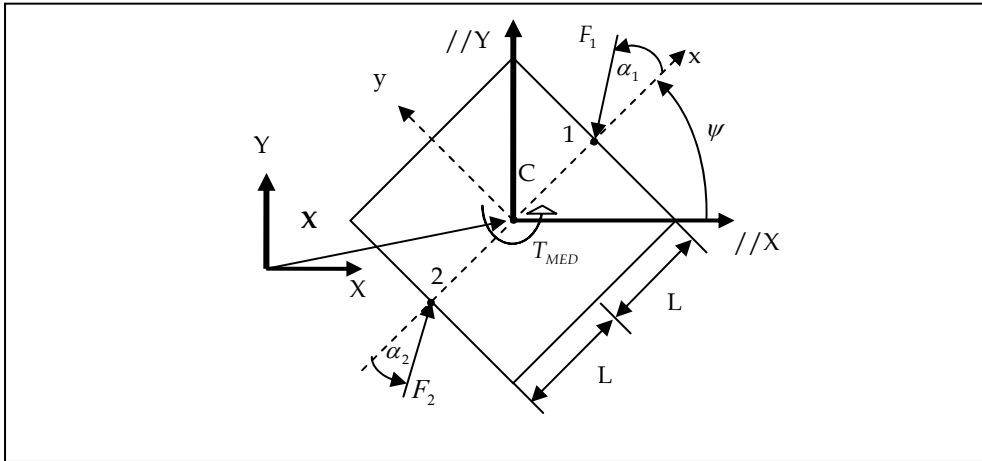


Fig. 3. SRL's 2nd Generation Spacecraft Simulator Schematic

The translation and attitude motion of the simulator are governed by the equations

$$\begin{aligned}
 \dot{\mathbf{X}} &= \mathbf{V} \\
 \dot{\mathbf{V}} &= m^{-1} {}^I \mathbf{R}_B(\psi) {}^B \mathbf{F} \\
 \dot{\psi} &= \omega_z \\
 \dot{\omega}_z &= J_z^{-1} {}^B T
 \end{aligned} \tag{1}$$

where  ${}^B \mathbf{F} \in \mathbb{R}^2$  are the thruster inputs limited to the region  $\pm\pi/2$  with respect to each face normal and  ${}^B T \in \mathbb{R}$  is the attitude input.  ${}^I \mathbf{R}_B(\psi)$ ,  ${}^B \mathbf{F}$  and  ${}^B T$  are given by

$${}^I \mathbf{R}_B(\psi) = \begin{bmatrix} c\psi & -s\psi \\ s\psi & c\psi \end{bmatrix} \tag{2}$$

$${}^B \mathbf{F}^T = {}^B \mathbf{F}_1^T + {}^B \mathbf{F}_2^T = [-F_1 c\alpha_1 + F_2 c\alpha_2, -F_1 s\alpha_1 + F_2 s\alpha_2]^T \tag{3}$$

$${}^B T = [T_{MED} + L(-F_1 s\alpha_1 - F_2 s\alpha_2)] \tag{4}$$

where  $s\bullet = \sin(\bullet)$ ,  $c\bullet = \cos(\bullet)$ .

The internal dynamics of the vectorable thrusters are assumed to be linear according to the following equations

$$\dot{\alpha}_1 = \beta_1, \dot{\beta}_1 = J_1^{-1} T_1, \dot{\alpha}_2 = \beta_2, \dot{\beta}_2 = J_2^{-1} T_2 \tag{5}$$

where  $J_1$  and  $J_2$  represent the moments of inertia about each thruster rotational axis respectively and  $T_1 \in \mathbb{R}$ ,  $T_2 \in \mathbb{R}$  represent the corresponding thruster rotation control input. The system's state equation given by Eq. (1) can be rewritten in control-affine system form as (LaValle, 2006)

$$\dot{\mathbf{x}} = \mathbf{f}(\mathbf{x}) + \sum_{i=1}^{N_u} u_i \mathbf{g}_i(\mathbf{x}) = \mathbf{f}(\mathbf{x}) + G(\mathbf{x})\mathbf{u}, \mathbf{x} \in \mathbb{R}^{N_x} \tag{6}$$

where  $N_u$  is the number of controls. With  $\mathbb{R}^{N_x}$  representing a smooth  $N_x$ -dimensional manifold defined by the size of the state-vector and the control vector to be in  $\mathbb{R}^{N_u}$ . Defining the state vector  $\mathbf{x} \in \mathbb{R}^{10}$  as  $\mathbf{x}^T = [x_1, x_2, \dots, x_{10}] = [X, Y, \psi, \alpha_1, \alpha_2, V_x, V_y, \omega_z, \beta_1, \beta_2]$  and the control vector  $\mathbf{u} \in \mathbb{U}^5$  as  $\mathbf{u}^T = [u_1, u_2, \dots, u_5] = [F_1, F_2, T_{MED}, T_1, T_2]$ , the system's state equation, becomes

$$\dot{\mathbf{x}} = \mathbf{f}(\mathbf{x}) + G(\mathbf{x})\mathbf{u} = [x_6, x_7, x_8, x_9, x_{10}, \mathbf{0}_{1 \times 5}]^T + \begin{bmatrix} \mathbf{0}_{5 \times 5} \\ G_1(\mathbf{x}) \end{bmatrix} \mathbf{u} \tag{7}$$

where the matrix  $G_1(\mathbf{x})$  is obtained from Eq. (1) as

$$G_1(\mathbf{x}) = \begin{bmatrix} -m^{-1}[cx_3 cx_4 - sx_3 sx_4] & m^{-1}[cx_3 cx_5 - sx_3 sx_5] & 0 & 0 & 0 \\ -m^{-1}[cx_3 sx_4 + sx_3 cx_4] & m^{-1}[cx_3 sx_5 + sx_3 cx_5] & 0 & 0 & 0 \\ -J_z^{-1} sx_4 L & -J_z^{-1} sx_5 L & J_z^{-1} & 0 & 0 \\ 0 & 0 & 0 & J_2^{-1} & 0 \\ 0 & 0 & 0 & 0 & J_2^{-1} \end{bmatrix} \tag{8}$$

With the system in the form of Eq. (6) given the vector fields in Eqs. (7) and (8), and given that  $\mathbf{f}(\mathbf{x})$  (the drift term) and  $G(\mathbf{x})$  (the control matrix of control vector fields) are smooth functions, it is important to note that it is not necessarily possible to obtain zero velocity due to the influence of the drift term. This fact places the system in the unique subset of control-affine systems with drift and, as seen later, will call for an additional requirement for determining the controllability of the system. Furthermore, when studying controllability of systems, the literature to date restricts the consideration to cases where the control is proper. Having a proper control implies that the affine hull of the control space is equal to  $\mathbb{R}^{N_u}$  or that the smallest subspace of  $\mathbb{U}$  is equal to the number of control vectors and that it is closed (Sussman, 1987; Sussman, 1990; Bullo & Lewis, 2005; LaValle, 2006). With a system such as a spacecraft in general or the simplified model of the 3-DoF simulator in particular, the use of on-off cold-gas thrusters restrict the control space to only positive space with respect to both thrust vectors leading to an unclosed set and thus improper control space. In order to overcome this issue, a method which leverages the symmetry of the system is used by which the controllability of the system is studied by considering only one virtual rotating thruster that is positioned a distance  $L$  from the center of mass with the vectored thrust resolved into a  $y$  and  $x$ -component. In considering this system perspective, the thruster combination now spans  $\mathbb{R}^2$  and therefore is proper and is analogous to the planar body with variable-direction force vector considered in (Lewis & Murray, 1997; Bullo & Lewis, 2005). Furthermore, under the assumption that the control bandwidth of the thrusters's rotation is much larger than the control bandwidth of the system dynamics, the internal dynamics of the vectorable thrusters can be decoupled from the state and control vectors for the system yielding a thrust vector dependent on simply a commanded angle. Thus the system's state vector, assuming that both thrusters and a momentum exchange device are available,

becomes  $\mathbf{x}^T = [x_1, x_2, \dots, x_6] = [X, Y, \psi, V_x, V_y, \omega_z] \in \mathbb{R}^6$  and the control vector is  $\mathbf{u}^T = [u_1, u_2, u_3] = [{}^B F_x, {}^B F_y, {}^B T_z] = \mathbf{U}^3$  so that the system's state equation becomes

$$\dot{\mathbf{x}} = \mathbf{f}(\mathbf{x}) + G(\mathbf{x})\mathbf{u} = [x_4, x_5, x_6, 0, 0, 0]^T + \begin{bmatrix} \mathbf{0}_{3 \times 3} \\ G_1(\mathbf{x}) \end{bmatrix} \mathbf{u} \quad (9)$$

where the matrix  $G_1(\mathbf{x})$  can be obtained by considering the relation of the desired control vector to the body centered reference system, in the two cases of positive force needed in the  $x$  direction ( ${}^B U_x > 0$ ) and negative force needed in the  $x$  direction ( ${}^B U_x < 0$ ). In this manner, the variables in Eq. (8) and Eq. (9) can be defined as

$$\begin{aligned} {}^B U_x < 0 &\rightarrow \begin{cases} \mathbf{u}^T = [{}^B F_x, {}^B F_y, {}^B T_z] = [-F_1 c x_4, -F_1 s x_4, T_{MED}] \\ d = -L, F_2 = 0 \end{cases} \\ {}^B U_x > 0 &\rightarrow \begin{cases} \mathbf{u}^T = [{}^B F_x, {}^B F_y, {}^B T_z] = [F_2 c x_5, F_2 s x_5, T_{MED}] \\ d = L, F_1 = 0 \end{cases} \end{aligned} \quad (10)$$

yielding the matrix in  $G_1(\mathbf{x})$  through substitution into Eq. (8) as

$$G_1(\mathbf{x}) = \begin{bmatrix} m^{-1} c x_3 & -m^{-1} s x_3 & 0 \\ m^{-1} s x_3 & m^{-1} c x_3 & 0 \\ 0 & -d J_z^{-1} & J_z^{-1} \end{bmatrix} \quad (11)$$

When the desired control input to the system along the body  $x$ -axis is zero, both thrusters can be used to provide a control force along the  $y$ -axis, while a momentum exchange device provides any required torque. In this case, the control vector in (9) becomes  $\mathbf{u}^T = [u_1, u_2] = [{}^B F_y, {}^B T_z] = \mathbf{U}^2$  such that the variables in Eq. (8) and (9) can be defined as

$${}^B U_x = 0 \rightarrow \begin{cases} \mathbf{u}^T = [{}^B F_y, {}^B T_z] = [F s \alpha, T_{MED}] \\ F = F_1 = F_2, \alpha = x_4 = -x_5 = -\frac{\pi}{2} \text{sign}({}^B U_y) \end{cases} \quad (12)$$

which yields the matrix  $G_1(\mathbf{x})$  through substitution into Eq. (8) as

$$G_1(\mathbf{x}) = \begin{bmatrix} -2m^{-1} s x_3 & 0 \\ 2m^{-1} c x_3 & 0 \\ 0 & J_z^{-1} \end{bmatrix} \quad (13)$$

As will be demonstrated in later, the momentum exchange device is not necessary to ensure small time controllability for this system. In considering this situation, which also occurs when a control moment gyroscope is present but is near the singular conditions and therefore requires desaturation, the thruster not being used for translation control can be slewed to  $\pm\pi/2$  depending on the required torque compensation and fired to affect the desired angular rate change. The desired control input to the system with respect to the body x-axis ( ${}^B U_x$ ) can again be used to define the desired variables such that

$$\begin{aligned}
 {}^B U_x \leq 0 &\rightarrow \begin{cases} \mathbf{u}^T = [{}^B F_x, {}^B F_y, {}^B T_z] = [-F_1 c x_4, -F_1 s x_4, F_2 d s x_5] \\ d = -L, x_5 = \pm \frac{\pi}{2} \end{cases} \\
 {}^B U_x > 0 &\rightarrow \begin{cases} \mathbf{u}^T = [{}^B F_x, {}^B F_y, {}^B T_z] = [F_2 c x_5, F_2 s x_5, -F_1 d s x_4] \\ d = L, x_4 = \pm \frac{\pi}{2} \end{cases}
 \end{aligned} \tag{14}$$

which yields the matrix  $G_1(\mathbf{x})$  through substitution into Eq. (8) as

$$G_1(\mathbf{x}) = \begin{bmatrix} m^{-1} c x_3 & -m^{-1} s x_3 & -(md)^{-1} s x_3 \\ m^{-1} s x_3 & m^{-1} c x_3 & (md)^{-1} c x_3 \\ 0 & -d J_z^{-1} & J_z^{-1} \end{bmatrix} \tag{15}$$

In case of zero force requested along x with only thrusters acting, the system cannot in general provide the requested torque value.

A key design consideration with this type of control actuator configuration is that with only the use of an on/off rotating thruster to provide the necessary torque compensation, fine pointing can be difficult and more fuel is required to affect a desired maneuver involving both translation and rotation.

#### 4. Small-Time Local Controllability

Before studying the controllability for a nonlinear control-affine system of the form in Eq. (6), it is important to review several definitions. First, the set of states reachable in time at most  $T$  is given by  $R_{\Sigma}(\mathbf{x}_0, \leq T)$  by solutions of the nonlinear control-affine system.

Definition 1 (Accessibility)

A system is *accessible* from  $\mathbf{x}_0$  (the initial state) if there exists  $T > 0$  such that the interior of  $R_{\Sigma}(\mathbf{x}_0, \leq t)$  is not an empty set for  $t \in ]0, T]$  (Bullo & Lewis, 2005).

Definition 2 (Proper Small Time Local Controllability)

A system is *small time locally controllable* (STLC) from  $\mathbf{x}_0$  if there exists  $T > 0$  such that  $\mathbf{x}_0$  lies in the interior of  $R_{\Sigma}(\mathbf{x}_0, \leq t)$  for each  $t \in ]0, T]$  for every proper control set  $U$  (Bullo &

Lewis, 2005). Assuming that at  $\mathbf{x}(0) = \mathbf{0}$  this can also be seen under time reversal as the equilibrium for the system  $x_0$  can be reached from a neighborhood in small time (Sussman, 1987; Sussman, 1990).

**Definition 3** (Proper Control Set) A control set  $\mathbf{u}^T = [u_1, \dots, u_k]$  is termed to be *proper* if the set satisfies a constraint  $\mathbf{u} \in K$  where  $K$  affinely spans  $U^k$ . (Sussman, 1990; Bullo & Lewis, 2005; LaValle, 2006).

**Definition 4** (Lie derivative) The *Lie derivative* of a smooth scalar function  $g(\mathbf{x}) \in \mathbb{R}$  with respect to a smooth vector field  $\mathbf{f}(\mathbf{x}) \in \mathbb{R}^{N_x}$  is a scalar function defined as (Slotine, 1991, pg. 229)

$$L_{\mathbf{f}}g = \nabla g \mathbf{f} = \begin{bmatrix} \frac{\partial g}{\partial x_1} & \dots & \frac{\partial g}{\partial x_{N_x}} \end{bmatrix} \begin{bmatrix} f_1(\mathbf{x}) \\ \vdots \\ f_{N_x}(\mathbf{x}) \end{bmatrix}. \quad (16)$$

**Definition 5** (Lie Bracket): The Lie bracket of two vector fields  $\mathbf{f}(\mathbf{x}) \in \mathbb{R}^{N_x}$  and  $\mathbf{g}(\mathbf{x}) \in \mathbb{R}^{N_x}$  is a third vector field  $[\mathbf{f}, \mathbf{g}] \in \mathbb{R}^{N_x}$  defined by  $[\mathbf{f}, \mathbf{g}] = \nabla \mathbf{g} \mathbf{f} - \nabla \mathbf{f} \mathbf{g}$ , where the  $i$ -th component can be expressed as (Slotine, 1991)

$$[\mathbf{f}, \mathbf{g}]_i = \sum_{j=1}^{N_x} \left( f_j \frac{\partial g_i}{\partial x_j} - g_j \frac{\partial f_i}{\partial x_j} \right). \quad (17)$$

Using Lie bracketing methods which produce motions in directions that do not seem to be allowed by the system distribution, sufficient conditions can be met to determine a system's STLTC even in the presence of a drift vector as in the equations of motion developed above. These sufficient conditions involve the Lie Algebra Rank Condition (LARC).

**Definition 6** (Associated Distribution  $\Delta(\mathbf{x})$ ) Given a system as in Eq. (6), the associated distribution  $\Delta(\mathbf{x})$  is defined as the vector space (subspace of  $\mathbb{R}^{N_x}$ ) spanned by the system vector fields  $\mathbf{f}, \mathbf{g}_1, \dots, \mathbf{g}_{N_u}$ .

**Definition 7** The Lie algebra of the associated distribution  $\mathcal{L}(\Delta)$  is defined to be the distribution of all independent vector fields that can be obtained by applying subsequent Lie bracket operations to the system vector fields. Of note, no more than  $N_x$  vector fields can be produced (LaValle, 2006). With  $\dim(\mathcal{L}(\Delta)) \leq N_x$ , the computation of the elements of  $\mathcal{L}(\Delta)$  ends either when  $N_x$  independent vector fields are obtained or when all subsequent Lie brackets are vector fields of zeros.

**Definition 8** (Lie Algebra Rank Condition (LARC)) The *Lie Algebra Rank Condition* is satisfied at a state  $\mathbf{x}$  if the rank of the matrix obtained by concatenating the vector fields of the Lie algebra distribution at  $\mathbf{x}$  is equal to  $N_x$  (the number of state).

For a driftless control-affine system, following the Chow-Rashevskii Theorem, the system is STLTC if the LARC is satisfied (Lewis & Murray, 1997; Bullo & Lewis, 2005; LaValle, 2006). However, given a system with drift, in order to determine the STLTC, the satisfaction of the

LARC it is not sufficient: in addition to the LARC, it is necessary to examine the combinations of the vectors used to compose the Lie brackets of the Lie algebra. From Sussman’s General Theorem on Controllability, if the LARC is satisfied and if there are no ill formed brackets in  $\mathcal{L}(\Delta)$ , then the system is STLC from its equilibrium point (Sussman, 1987). The Sussman’s theorem, formally stated is reported here below.

**Theorem 1** (Sussman’s General Theorem on Controllability) Consider a system given by Eq. (6) and an equilibrium point  $\mathbf{p} \in \mathbb{R}^{N_s}$  such that  $\mathbf{f}(\mathbf{p}) = \mathbf{0}$ . Assume  $\mathcal{L}(\Delta)$  satisfies the LARC at  $\mathbf{p}$ . Furthermore, assume that whenever a potential Lie bracket consists of the drift vector  $\mathbf{f}(\mathbf{x})$  appearing an odd number of times while  $\mathbf{g}_1(\mathbf{x}), \dots, \mathbf{g}_{N_u}(\mathbf{x})$  all appear an even number of times to include zero times (indicating an ill formed Lie bracket), there are sufficient successive Lie brackets to overcome this ill formed Lie bracket to maintain LARC. Then the system is STLC from  $\mathbf{p}$ . (Sussman, 1987; Sussman, 1990).

As it is common in literature, an ill formed bracket is dubbed a “bad” bracket (Sussman, 1987; Sussman, 1990; Lewis & Murray, 1997, Bullo & Lewis, 2005; LaValle, 2006). Conversely, if a bracket is not “bad”, it is termed “good”. As an example, for a system with a drift vector and two control vectors, the bracket  $[\mathbf{f}, [\mathbf{g}_1, \mathbf{g}_1]]$  is bad, as the drift vector occurs only once while the first control vector appears twice and the second control vector appears zero times. Similarly, the bracket  $[\mathbf{f}, [\mathbf{f}, [\mathbf{f}, \mathbf{g}_1]]]$  is good as the first control vector appears only once. Therefore, it can be summarized that if the rank of the Lie algebra of a control-affine system with drift is equal to the number of states and there exist sufficient “good” brackets to overcome the “bad” brackets to reach the required LARC rank, then the system is small time locally controllable.

#### 4.1 Small-Time Local Controllability Considerations for the 3-DoF Spacecraft Simulator

The concept of small time local controllability is better suitable than the one of accessibility for the problem of spacecraft rendezvous and docking, as a spacecraft is required to move in any directions in a small interval of time dependent on the control actuator capabilities (e.g. to avoid obstacles). The finite time  $T$  can be arbitrary if the control input is taken to be unbounded and proper (Sussman, 1990; Bullo & Lewis, 2005; LaValle, 2006).

While no theory yet exists for the study of the general controllability for a non-linear system, the STLC from an equilibrium condition can be studied by employing Sussman’s theorem. For the case of spacecraft motion, in order to apply Sussman’s theorem, we hypothesize that the spacecraft is moving from an initial condition with velocity close to zero (relative to the origin of an orbiting reference frame).

In applying Sussman’s General Theorem on Controllability to the reduced system equations of motion presented in Eq. (9) with  $G_1(\mathbf{x})$  given in Eq. (11), the Lie algebra evaluates to

$$\mathcal{L}(\Delta) = span\{\mathbf{g}_1, \mathbf{g}_2, \mathbf{g}_3, [\mathbf{f}, \mathbf{g}_1], [\mathbf{f}, \mathbf{g}_2], [\mathbf{f}, \mathbf{g}_3]\} \tag{18}$$

so that  $\dim(\mathcal{L}(\Delta)) = N_x = 6$ . In order to verify that this is the minimum number of actuators required to ensure STLC, the Lie algebra is reinvestigated for each possible combination of controls. The resulting analysis, as summarized in **Table 2**, demonstrates that the system is STLC from the systems equilibrium point at  $\mathbf{x}_0 = \mathbf{0}$  given either two rotating thrusters in complementary semi-circle planes or fixed thrusters on opposing faces providing a normal force vector to the face in opposing directions and a momentum exchange device about the center of mass. For instance, in considering the case of control inputs  ${}^B F_y, {}^B T_z = T_{MED}$ , Eq. (9) becomes

$$\begin{aligned} \dot{\mathbf{x}} &= \mathbf{f}(\mathbf{x}) + \mathbf{g}_1(\mathbf{x})u_1 + \mathbf{g}_2(\mathbf{x})u_2 \\ &= [x_4, x_5, x_6, 0, 0, 0]^T + [0, 0, 0, m^{-1}sx_3, m^{-1}cx_3, J_z^{-1}L]^T u_1 + [0, 0, 0, 0, 0, J_z^{-1}]^T u_2 \end{aligned} \tag{19}$$

where  $\mathbf{u} = [u_1, u_2] = [{}^B F_y, {}^B T_z] \in \mathbb{U}^2$ . The equilibrium point  $\mathbf{p}$  such that  $\mathbf{f}(\mathbf{p}) = \mathbf{0}$  is  $\mathbf{p} = [x_1, x_2, x_3, 0, 0, 0]^T$ . The  $\mathcal{L}(\Delta)$  is formed by considering the associated distribution  $\Delta(\mathbf{x})$  and successive Lie brackets as

$$\begin{array}{lll} \mathbf{f}, & \mathbf{g}_1, & \mathbf{g}_2 \\ [\mathbf{f}, \mathbf{g}_1], & [\mathbf{g}_1, \mathbf{g}_2], & [\mathbf{f}, \mathbf{g}_2] \\ [\mathbf{f}, [\mathbf{f}, \mathbf{g}_1]], & [\mathbf{f}, [\mathbf{g}_1, \mathbf{g}_2]], & [\mathbf{f}, [\mathbf{f}, \mathbf{g}_2]], \\ [\mathbf{g}_1, [\mathbf{f}, \mathbf{g}_1]], & [\mathbf{g}_1, [\mathbf{g}_1, \mathbf{g}_2]], & [\mathbf{g}_1, [\mathbf{f}, \mathbf{g}_2]], \\ [\mathbf{g}_2, [\mathbf{f}, \mathbf{g}_1]], & [\mathbf{g}_2, [\mathbf{g}_1, \mathbf{g}_2]], & [\mathbf{g}_2, [\mathbf{f}, \mathbf{g}_2]], \\ [\mathbf{f}, [\mathbf{f}, [\mathbf{f}, \mathbf{g}_1]]], & [\mathbf{f}, [\mathbf{f}, [\mathbf{g}_1, \mathbf{g}_2]]], & [\mathbf{f}, [\mathbf{f}, [\mathbf{f}, \mathbf{g}_2]]], \quad [\mathbf{f}, [\mathbf{g}_1, [\mathbf{f}, \mathbf{g}_1]]] \end{array}$$

The sequence can first be reduced by considering any “bad” brackets in which the drift vector appears an odd number of times and the control vector fields each appear an even number of times to include zero. In this manner the Lie brackets  $[\mathbf{g}_1, [\mathbf{f}, \mathbf{g}_1]]$  and  $[\mathbf{g}_2, [\mathbf{f}, \mathbf{g}_2]]$  can be disregarded.

By evaluating each remaining Lie bracket at the equilibrium point  $\mathbf{p}$ , the linearly independent vector fields can be found as

$$\begin{aligned} \mathbf{g}_1 &= [0, 0, 0, -m^{-1}sx_3, m^{-1}cx_3, -J_z^{-1}L]^T \\ \mathbf{g}_2 &= [0, 0, 0, 0, 0, J_z^{-1}]^T \\ [\mathbf{f}, \mathbf{g}_1] &= \nabla \mathbf{g}_1 \cdot \mathbf{f} - \nabla \mathbf{f} \cdot \mathbf{g}_1 = [m^{-1}sx_3, -m^{-1}cx_3, -J_z^{-1}L, 0, 0, 0]^T \\ [\mathbf{f}, \mathbf{g}_2] &= \nabla \mathbf{g}_2 \cdot \mathbf{f} - \nabla \mathbf{f} \cdot \mathbf{g}_2 = [0, 0, -J_z^{-1}, 0, 0, 0]^T \\ [\mathbf{g}_1, [\mathbf{f}, \mathbf{g}_2]] &= \nabla [\mathbf{f}, \mathbf{g}_2] \cdot \mathbf{g}_1 - \nabla \mathbf{g}_1 \cdot [\mathbf{f}, \mathbf{g}_2] = [0, 0, 0, -m^{-1}J_z^{-1}cx_3, -m^{-1}J_z^{-1}sx_3, 0]^T \\ [\mathbf{f}, [\mathbf{g}_1, [\mathbf{f}, \mathbf{g}_1]]] &= \nabla [\mathbf{g}_1, [\mathbf{f}, \mathbf{g}_1]] \cdot \mathbf{f} - \nabla \mathbf{f} \cdot [\mathbf{g}_1, [\mathbf{f}, \mathbf{g}_1]] = [2Lm^{-1}J_z^{-1}cx_3, 2Lm^{-1}J_z^{-1}sx_3, 0, 0, 0, 0]^T \end{aligned} \tag{20}$$

Therefore, the Lie algebra comprised of these vector fields is

$$\mathcal{L}(\Delta) = \text{span}\{\mathbf{g}_1, \mathbf{g}_2, [\mathbf{f}, \mathbf{g}_1], [\mathbf{f}, \mathbf{g}_2], [\mathbf{g}_1, [\mathbf{f}, \mathbf{g}_2]], [\mathbf{f}, [\mathbf{g}_1, [\mathbf{f}, \mathbf{g}_1]]]\} \tag{21}$$

yielding  $\dim(\mathcal{L}(\Delta)) = N_x = 6$ , and therefore the system is small time locally controllable.

Control	Thruster Positions	$\dim(\mathcal{L}(\Delta))$	Controllability
$\mathbf{u}^T = [{}^B F_x, 0, 0]$	$\alpha_1 = \alpha_2 = 0$	2	Inaccessible
$\mathbf{u}^T = [0, {}^B F_y, 0]$	$\alpha_1 = -\alpha_2 = \mp \pi/2$	2	Inaccessible
$\mathbf{u}^T = [0, 0, {}^B T_z]$	NA	2	Inaccessible
$\mathbf{u}^T = [0, {}^B F_y, {}^B T_z = F_j L s \alpha_j]$	$\alpha_i = \mp \pi/2, \alpha_j = \pm \pi/2$	5	Inaccessible
$\mathbf{u}^T = [{}^B F_x, {}^B F_y, 0]$	$ \alpha_1  \leq \pi/2,  \alpha_2  \leq \pi/2$	6	STLC
$\mathbf{u}^T = [{}^B F_x, 0, {}^B T_z]$	$\alpha_1 = \alpha_2 = 0$	6	STLC
$\mathbf{u}^T = [0, {}^B F_y, {}^B T_z = T_{MED}]$	$\alpha_1 = -\alpha_2 = \mp \pi/2$	6	STLC

Table 2. STLC Analysis for the 3-DoF Spacecraft Simulator

### 5. Navigation and Control of the 3-DoF Spacecraft Simulator

In the current research, the assumption is made that the spacecraft simulator is maneuvering in the proximity of an attitude stabilized target spacecraft and that this spacecraft follows a Keplerian orbit. Furthermore, the proximity navigation maneuvers are considered to be fast with respect to the orbital period. A pseudo-GPS inertial measurement system by Metris, Inc. (iGPS) is used to fix the ICS in the laboratory setting for the development of the state estimation algorithm and control commands. The X-axis is taken to be the vector between the two iGPS transmitters with the Y and Z axes forming a right triad through the origin of a reference system located at the closest corner of the epoxy floor to the first iGPS transmitter. Navigation is provided by fusing of the magnetometer data and fiber optic gyro through a discrete Kalman filter to provide attitude estimation and through the use of a linear quadratic estimator to estimate the translation velocities given inertial position measurements. Control is accomplished through the combination of a state feedback linearized based controller, a linear quadratic regulator, Schmitt trigger logic and Pulse Width Modulation using the minimal control actuator configuration of the 3-DoF spacecraft simulator. Fig. 4 reports a block diagram representation of the control system.

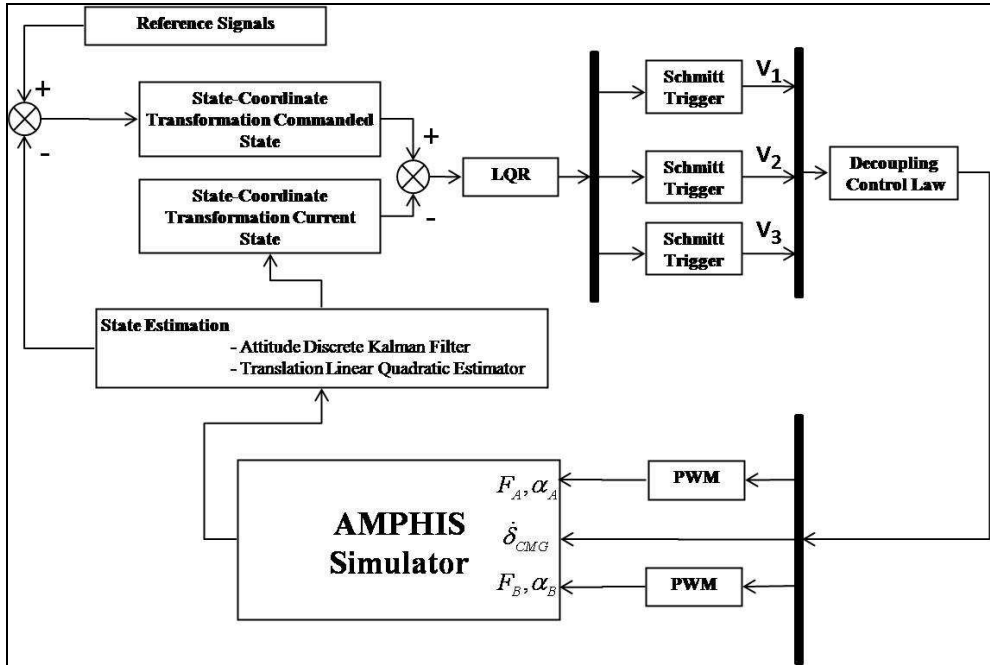


Fig. 4. Block Diagram of the Control System of the 3-DoF Spacecraft simulator

**5.1 Navigation using Inertial Measurements with Kalman Filter and Linear Quadratic Estimator**

In the presence of the high accuracy, low noise, high bandwidth iGPS sensor with position accuracy to within 5.4 mm with a standard deviation of 3.6 mm and asynchronous measurement availability with a nominal frequency of 40 Hz, a full-order linear quadratic estimator with respect to the translation states is implemented to demonstrate the capability to estimate the inertial velocities in the absence of accelerometers. Additionally, due to the affect of noise and drift rate in the fiber-optic gyro, a discrete-time linear Kalman filter is employed to fuse the data from the magnetometer and the gyro. Both the gyro and magnetometer are capable of providing new measurements asynchronously at 100 Hz.

**5.1.1 Attitude Discrete-Time Kalman Filter**

With the attitude rate being directly measured, the measurement process can be modeled in state-space equation form as:

$$\begin{bmatrix} \omega_z \\ \dot{\beta}_s \end{bmatrix} = \underbrace{\begin{bmatrix} 0 & -1 \\ 0 & 0 \end{bmatrix}}_A \begin{bmatrix} \psi \\ \beta_s \end{bmatrix} + \underbrace{\begin{bmatrix} 1 \\ 0 \end{bmatrix}}_B \omega_s + \underbrace{\begin{bmatrix} -1 & 0 \\ 0 & 1 \end{bmatrix}}_G \begin{bmatrix} \eta_{\omega_s} \\ \eta_{\beta_s} \end{bmatrix} \tag{22}$$

$$z = \psi_m = \underbrace{\begin{bmatrix} 1 & 0 \end{bmatrix}}_H \begin{bmatrix} \psi \\ \beta_s \end{bmatrix} + \eta_{\psi_m} \tag{23}$$

where  $\omega_g$  is the measured gyro rate,  $\beta_g$  is the gyro drift rate,  $\eta_{\omega_g}$  and  $\eta_{\beta_g}$  are the associated gyro output measurement noise and the drift rate noise respectively.  $\psi_m$  is the measured angle from the magnetometer, and  $\eta_{\psi_m}$  is the associated magnetometer output measurement noise. It is assumed that  $\eta_{\omega_g}$ ,  $\eta_{\beta_g}$  and  $\eta_{\psi_m}$  are zero-mean Gaussian white-noise processes with variances given by  $\sigma_{\omega_g}^2$ ,  $\sigma_{\beta_g}^2$  and  $\sigma_{\psi_m}^2$  respectively. Introducing the state variables  $\mathbf{x}^T = [\psi, \beta_g]$ , control variables  $u = \omega_g$ , and error variables  $\mathbf{w}^T = [\eta_{\omega_g}, \eta_{\beta_g}]$  and  $v = \eta_{\psi_m}$ , Eqs. (22) and (23) can be expressed compactly in matrix form as

$$\dot{\mathbf{x}}(t) = A(t)\mathbf{x}(t) + B(t)\mathbf{u}(t) + G(t)\mathbf{w}(t) \tag{24}$$

$$\mathbf{z}(t) = H\mathbf{x}(t) + \mathbf{v}(t) \tag{25}$$

In assuming a constant sampling interval  $\Delta t$  in the gyro output, the system equation Eq. (24) and observation equations Eq. (25) can be discretized and rewritten as

$$\mathbf{x}_{k+1} = \Phi_k \mathbf{x}_k + \Gamma_k \mathbf{u}_k + \Upsilon_k \mathbf{w}_k \tag{26}$$

$$\mathbf{z}_k = H_k \mathbf{x}_k + \mathbf{v}_k \tag{27}$$

where

$$\Phi_k = e^{A\Delta t} = \begin{bmatrix} 1 & -\Delta t \\ 0 & 1 \end{bmatrix} \tag{28}$$

and

$$\Gamma_k = \int_0^{\Delta t} e^{A\tau} B d\tau = \begin{bmatrix} \Delta t \\ 0 \end{bmatrix} \tag{29}$$

The process noise covariance matrix used in the propagation of the estimation error covariance given by (Gelb, 1974; Crassidis & Junkins, 2004)

$$(\Upsilon_k Q_k \Upsilon_k^T)^T = \int_{t_k}^{t_{k+1}} \int_{t_k}^{t_{k+1}} \Phi(t_{k+1}, \tau) G(\tau) E\{\mathbf{w}(\tau)\mathbf{w}^T(\alpha)\} G^T(\alpha) \Phi(t_{k+1}, \alpha) d\tau d\alpha \tag{30}$$

can be properly numerically estimated given a sufficiently small sampling interval by following the numerical solution by van Loan (Crassidis & Junkins, 2004). First, the following  $2n \times 2n$  matrix is formed:

$$\mathbf{a} = \begin{bmatrix} -A & GQ G^T \\ 0 & A^T \end{bmatrix} \Delta t \tag{31}$$

where  $\Delta t$  is the constant sampling interval,  $A$  and  $G$  are the constant continuous-time state matrix and error distribution matrix given in Eq. (24), and  $Q$  is the constant continuous-time process noise covariance matrix

## Thank You for previewing this eBook

You can read the full version of this eBook in different formats:

- HTML (Free /Available to everyone)
- PDF / TXT (Available to V.I.P. members. Free Standard members can access up to 5 PDF/TXT eBooks per month each month)
- Epub & Mobipocket (Exclusive to V.I.P. members)

To download this full book, simply select the format you desire below

